


Article

A State-of-Health Estimation Method of a Lithium-Ion Power Battery for Swapping Stations Based on a Transformer Framework

Yu Shi ¹, Haicheng Xie ², Xinhong Wang ¹, Xiaoming Lu ¹, Jing Wang ¹, Xin Xu ¹, Dingheng Wang ¹ and Siyan Chen ^{2,3,*} 

¹ Jilin State Power Economic and Technical Research Institute, Changchun 130022, China

² College of Automotive Engineering, Jilin University, Changchun 130022, China

³ State Key Laboratory of Automotive Chassis Integration and Bionic, Jilin University, Changchun 130022, China

* Correspondence: chensiyuan1987@jlu.edu.cn

Abstract: Against the backdrop of automobile electrification, an increasing number of battery-swapping stations for electric vehicles have been launched to address the issue of slow battery charging under cold temperature conditions. However, due to the separation of the discharging and charging processes for lithium-ion batteries (LIBs) at swapping stations, and the circulation of batteries across different vehicles and stations, the operating data become fragmented, making it difficult to accurately identify the battery state-of-health (SOH). This study proposes a BiLSTM-Transformer framework that extracts the Constant Voltage Time (CVT) feature using only charging data, enabling the precise estimation of battery capacity degradation. Validation experiments conducted on battery samples under different operating temperatures showed that the model achieved a normalized RMSE of less than 1.6%. In ideal conditions, the normalized RMSE of the estimation reached as low as 0.11%. This model enables SOH estimation without relying on discharge data, contributing to the efficient and safe operation of battery swapping stations.

Keywords: lithium-ion battery; capacity estimation; transformer framework; swapping stations; multi-feature analysis



Academic Editor: Rodolfo Dufo-López

Received: 3 December 2024

Revised: 27 December 2024

Accepted: 9 January 2025

Published: 11 January 2025

Citation: Shi, Y.; Xie, H.; Wang, X.; Lu, X.; Wang, J.; Xu, X.; Wang, D.; Chen, S. A State-of-Health Estimation Method of a Lithium-Ion Power Battery for Swapping Stations Based on a Transformer Framework. *Batteries* **2025**, *11*, 22. <https://doi.org/10.3390/batteries11010022>

Copyright: © 2025 by the authors. Licensee MDPI, Basel, Switzerland. This article is an open access article distributed under the terms and conditions of the Creative Commons Attribution (CC BY) license (<https://creativecommons.org/licenses/by/4.0/>).

1. Introduction

The electrification of vehicles is accelerating under the global wave of advancing carbon neutrality targets. Governments in many countries and regions are actively promoting the transition to low-carbon development in the public transportation sector, and operational vehicles such as buses, cabs and internet taxis are being converted to purely electric vehicles on a large scale. However, the problems of a long charging time and low replenishment efficiency of operational vehicles are still restricting the promotion and application of electric vehicles.

Solving the problem of slow charging of electric vehicles, power batteries adapted to 4C and 5C charging multipliers have come into being, compressing the replenishment time to less than 20 min [1]. However, in cold regions, the application of fast charging technology is greatly restricted. Studies have shown that battery aging is closely related to the use of the environment, especially in cold regions, where a low temperature exacerbates the internal aging side reactions of the battery, resulting in a significantly higher rate of capacity degradation than in warmer regions [2,3]. In addition, the internal material diffusion

capacity of the battery decreases under a low temperature, and when rapid charging, the battery terminal voltage rises rapidly to reach the charging cut-off voltage, while also increasing the risk of lithium metal deposition [4,5]. These factors seriously restrict the application of fast charging technology in cold regions. In the electric vehicle power battery-swapping technology, the batteries are rotated and have enough time for maintenance, and each battery pack has enough time for charging and maintenance; therefore, it receives special attention in the cold region [6–8].

For a shared power battery, its safety and reliability are especially important, and if a battery fire accident occurs, the damage caused by it is often more serious. However, in the application scenario of power batteries, LIBs are not fully depleted, which makes it difficult to obtain the SOH through full charging/discharging. In addition, for electric vehicle charged by means of battery swapping, the power battery data are fragmented between the vehicle end and the swapping station. Moreover, a battery will rotate between different vehicles and different swapping stations, which makes the estimation of the battery SOH even more difficult. In the past, battery SOH estimations can be generally categorized into two types: model-based methods and data-driven methods. Model-based methods estimate battery capacity by updating parameters in a mathematical model of battery aging, such as empirical exponential models and ensemble empirical models [9,10]. These methods are usually combined with filtering algorithms to determine model parameters and predict capacity. However, their accuracy is highly dependent on the fidelity of the degradation model. In contrast, data-driven methods possess strong nonlinear mapping capabilities. Early battery SOH data-driven techniques utilized tools such as support vector machines [11] and neural networks [12–14]. With the advancement of artificial intelligence, more complex architectural neural networks have demonstrated superior performance in battery life prediction [15–17]. For example, the Bidirectional Long Short-Term Memory (BiLSTM) neural network, which processes both forward and backward information in a time series, is able to extract temporal features more comprehensively than unidirectional LSTMs, and is more effective in discovering potential patterns in battery capacity changes [18,19]. The Transformers framework, which incorporates a multi-attention mechanism, has a strong feature extraction capability and achieves excellent prediction on a variety of datasets [20,21].

Data-driven methods are usually inseparable from efficient characterization data. For example, the Incremental Capacity Analysis (ICA) method uses the characteristic signals related to the aging process of the negative electrode graphite to predict the capacity decay phenomenon of the battery based on the amount of voltage and current changes over time in the battery operation [22,23]. The Differential Thermal Voltammetry (DTV) method, on the other hand, further takes into account the temperature evolution process in the aging of the battery on the basis of the battery voltage and current data, and uses the battery temperature and battery voltage data to track the capacity degradation of the battery [24,25]. However, all of the above features are constructed using a differential approach, which tends to amplify the sensor error signal and reduce the accuracy and reliability of the SOH estimation method [26].

The long battery maintenance session in the swapping station is more suitable for battery capacity estimation, and the battery constant current and constant voltage (CC-CV) charging is much more stable than the dynamic operation of the discharging. Therefore, for battery capacity estimation in swapping stations, we construct the charging Constant Voltage Time feature (CVT), which is the constant-voltage charging duration at the end of the battery charging period. The CVT feature is not computed differentially, and it does not involve the battery discharging session. In addition, we propose the BiLSTM-Transformer deep learning framework based on the previous work, which combines the great processing

capability of the BiLSTM for temporal signals and the powerful feature extraction capability of the Transformer multi-head attention mechanism. In this research work, we only use the signals captured during the battery charging to build IC and CVT features, and combine the BiLSTM-Transformer deep learning technique to predict the capacity decay curve of the battery. The main contributions of this work are as follows:

1. Using charging data to extract CVT features with high correlation to battery capacity;
2. Build a BiLSTM-Transformer framework to combine robust time-series processing with feature extraction capability;
3. Battery aging experiments were designed to obtain aging datasets of batteries operating at room temperature and low temperature to validate the generalization ability of the model;
4. The model was trained using data from the first 40% of the battery lifecycle, enabling a highly accurate prediction of future capacity degradation trajectories.

2. Experiment and Feature Analysis

2.1. Experiment and Related Data

We selected 12 identical lithium-ion batteries (LIBs) for the cyclic aging experiment under different operating conditions, and the performance parameters of the pouch battery samples are shown in Table 1. Figure 1a shows the capacity decay trajectories of these batteries during the experiment, revealing significant differences in the decay trends under different conditions. Even if the batteries have the same operating conditions, e.g., #1, #2, the difference in the number of cycles is observed, which is due to the inconsistency between the batteries, and the inconsistency of the battery capacity decay trajectories poses a challenge for the generalization of the SOH estimation model, which requires the neural network to capture features with high correlation with the battery capacity decay.

Table 1. Battery sample parameters.

LIB Chemistry	Nominal Capacity	Standard Charge/Discharge Current	Maximum Charge/Discharge Current	Operational Voltage Range
NCM-Hard carbon	5000 mAh	3C (15 A)	10C (50 A)	2.8 V~4.2 V

The battery aging experiments were conducted at room temperature and low temperature to simulate the low-temperature charging scenarios that may be encountered by power batteries in power exchange stations in cold regions. All experimental groups used high rate charging/discharging currents, and the detailed experimental parameters are shown in Table 2. The initial capacities of the batteries at different temperatures are significantly different. For example, the capacity is significantly lower than the nominal 5 Ah and only about 4.6 Ah in the low temperature environment (0 °C). The phenomenon that this type of battery can discharge a decrease in capacity is attributed to the change of lithium-ion diffusion kinetics, especially the sharp decrease of solid-phase diffusion rate, which prevents the lithium-ions from embedding into the electrode material quickly. In turn, the change in lithium-ion kinetics leads to a rapid drop in the terminal voltage of the battery during the discharge process, as well as a premature termination of the discharge session. To solve this problem, a constant voltage (CV) discharge step was added to the low-temperature aging cycle to ensure that lithium-ions are fully embedded and de-embedded in the electrode materials of the battery, resulting in a consistent depth of charge and discharge of the battery for each experimental temperature condition. The

battery capacity in this study is based on the charging charge of each cycle. The 0 °C experimental group was also subjected to initial capacity calibration at 25 °C, whereas the initial capacity would slightly exceed the nominal 5000 mAh due to the added CV discharge step.

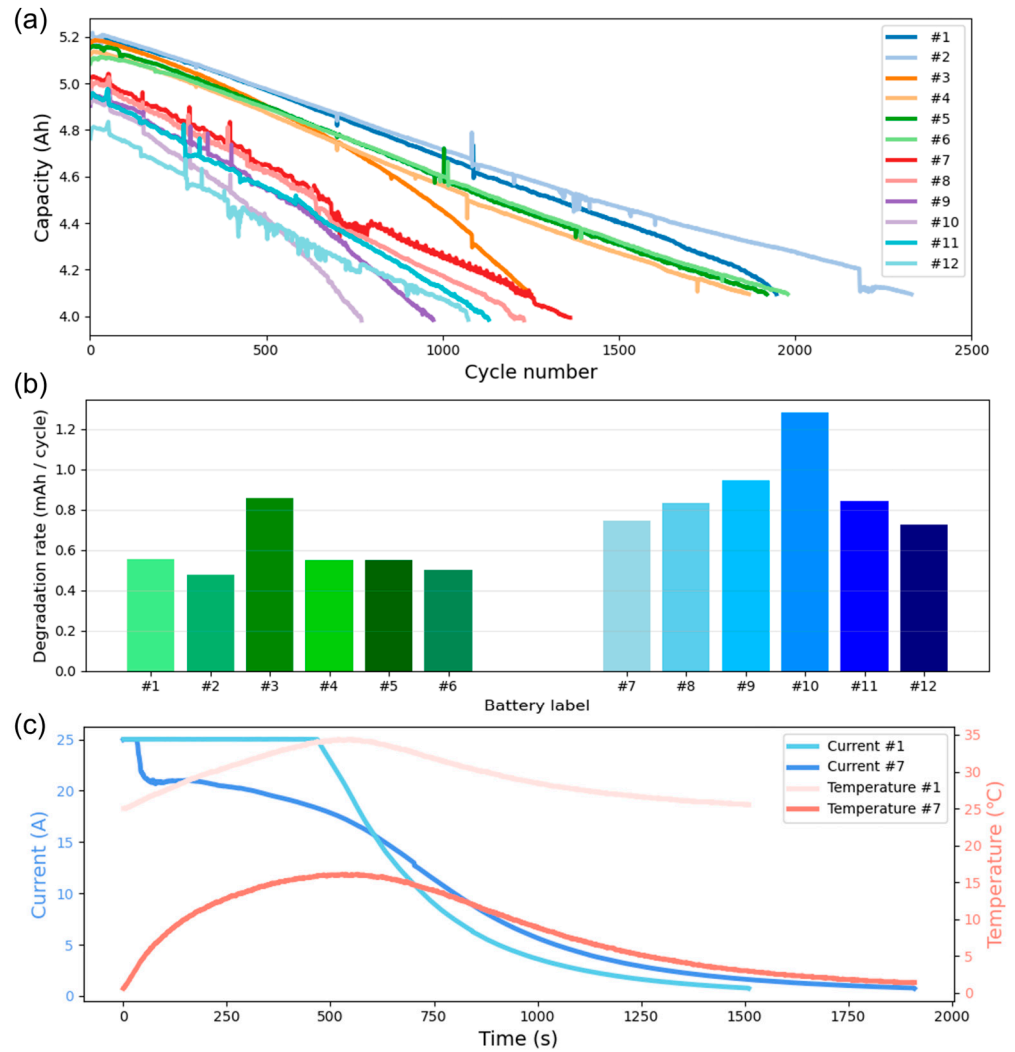


Figure 1. Experimental results. (a) Battery aging curve. (b) Number of cycles to 80% SOH at different temperatures. (c) Charging current and temperature curves at 0 °C vs. 25 °C.

Table 2. Experimental settings.

Label	Temperature	Charge Current	Discharge Current	Cut-Off Current	Voltage Range
#1	25 °C	5C (25 A)			
#2	25 °C	5C (25 A)			
#3	25 °C	4C (20 A)			
#4	25 °C	4C (20 A)			
#5	25 °C	3C (15 A)			
#6	25 °C	3C (15 A)			
#7	0 °C	5C (25 A)	3C (15 A)	3/20C (750 mA)	2.8 V~4.2 V
#8	0 °C	5C (25 A)			
#9	0 °C	4C (20 A)			
#10	0 °C	4C (20 A)			
#11	0 °C	3C (15 A)			
#12	0 °C	3C (15 A)			

Studies have shown that battery operating conditions (e.g., temperature and current) affect the battery capacity decay trajectory [27–29]. Table 3 demonstrates the number of cycles required to age the battery to 80% SOH under different conditions. It can be found that the number of cycles is significantly higher for batteries aged at room temperature than at low temperature (0 °C). In order to avoid the effect of inconsistency in the initial capacity of the battery on the number of cycles, the study proposes a single-cycle average loss of battery capacity, which is obtained by dividing the difference between the end-of-life (EoL) capacity of the battery and the initial capacity, by the number of cycles, as shown in Figure 1b. From the figure, the difference in battery aging rates at different temperatures can be clearly observed, and the accelerated aging of the battery at lower temperatures is attributed to the decrease in the lithium-ion diffusion rate. During charging at low temperatures, lithium-ions fail to embed in the anode in time, leading to elevated overpotential and lithium metal deposition. This phenomenon rapidly depletes a large amount of recyclable lithium-ions, leading to a rapid decay of the battery maximum capacity.

Table 3. Results of aging experiments.

Operation Temperature	Cells	Charging Rate	Cycles to EoL	SOH	Calibration Temperature	Capacity
25 °C	#1	5C (25 A)	1947	100% 80%	25 °C 25 °C	5175 mAh 4095 mAh
	#2	5C (25 A)	2330	100% 80%	25 °C 25 °C	5209 mAh 4095 mAh
	#3	4C (20 A)	1252	100% 80%	25 °C 25 °C	5167 mAh 4095 mAh
	#4	4C (20 A)	1870	100% 80%	25 °C 25 °C	5122 mAh 4095 mAh
	#5	3C (15 A)	1921	100% 80%	25 °C 25 °C	5153 mAh 4095 mAh
	#6	3C (15 A)	1979	100% 80%	25 °C 25 °C	5085 mAh 4095 mAh
0 °C	#7	5C (25 A)	1363	100% 80%	25/0 °C 25/0 °C	5019/5012 mAh 4624/3994 mAh
	#8	5C (25 A)	1232	100% 80%	25/0 °C 25/0 °C	5047/5009 mAh 4693/3983 mAh
	#9	4C (20 A)	975	100% 80%	25/0 °C 25/0 °C	4981/4904 mAh 4660/3985 mAh
	#10	4C (20 A)	771	100% 80%	25/0 °C 25/0 °C	5013/4970 mAh 4793/3982 mAh
	#11	3C (15 A)	1131	100% 80%	25/0 °C 25/0 °C	4996/4940 mAh 4762/3986 mAh
	#12	3C (15 A)	1074	100% 80%	25/0 °C 25/0 °C	4834/4763 mAh 4715/3985 mAh

In addition, there is a significant correlation between the decay path of a battery and its charging magnification. Previous studies have suggested that high current fast charging leads to accelerated battery capacity degradation, but we have newer findings in our experiments. The accelerated degradation due to fast charging at high current multiplication rates can be explained by the inability of lithium-ions to embed in the anode particles in a timely manner, leading to the precipitation of lithium metal or the fragmentation of the particles. As for cells #5 and #6 operating at 3C at 0 °C, the rate of capacity degradation is lower than that of cells #3 and #4 operating at 4C, as stated

in the findings of previous studies. However, when the charging current multiplier is further increased, a different phenomenon occurs, as the capacity decay rate of cells #1 and #2 operating at 5C is also lower than that of cells #3 and #4 operating at 4C, which is believed to be due to the fact that the increase in cell temperature brought about by the high current multiplier improves the lithium-ion diffusion performance and reduces the probability of the occurrence of the aging side reactions inside the cells. Figure 1c gives the curves of battery voltage and temperature over time in charging. In the figure, the CC charging time of cell #7 working at 0 °C is short due to the limitation of lithium-ion anode diffusion, and the battery terminal voltage rises rapidly to 4.2 V. However, when the battery temperature rises, the current of the CV charging session of the battery decreases slowly (100 s~750 s), and the change of temperature rise on the internal chemical reaction conditions of the battery improves the rapid decay of the battery capacity induced by the low temperature, so that the cells #7 and #8 (5C charge) have a lower aging rate than cells #9 and #10 (4C charge).

The capacity degradation of most battery samples shows an obvious linear relationship. However, the single-cycle capacity decay rate of #3 and #10 gradually increases with the number of cycles (the slope of the capacity–cycle curve decreases), as shown in Figure 1a, i.e., the phenomenon of “Knee” occurs [30]. The appearance of Knee greatly increases the degree of nonlinearity of the aging process, prompting the battery to rapidly reach the EoL [31]. Knee is not only related to the use of operating conditions, but also related to the internal inconsistency of the battery. In Figure 1c, the capacity decay rate of the battery charged at 4C at 0 °C is higher than that of the battery charged at 5C and 3C, and the faster rate of capacity decay exacerbates the probability of the battery to develop Knee. At 25 °C, there is almost no difference in the aging rate of the batteries under each charging multiplication rate except for the #3 sample, but #3 shows an obvious accelerated aging phenomenon. The inconsistency of cell #3 itself leads to the occurrence of the Knee phenomenon. Whichever causes the Knee phenomenon, it will lead to an increase in the nonlinearity of the battery capacity decay trajectory, which increases the difficulty of estimating the SOH.

2.2. Multi-Feature Analysis

When lithium-ion batteries are used as on-board power batteries, pure electric vehicles will not be fully depleted during driving, resulting in difficulty in obtaining the SOH of the battery through full charge/discharge, which often needs to be estimated by using features combined with neural network algorithms. For power batteries, by swapping to replenish energy, the battery data are scattered between the vehicle and swapping station, and there is a certain degree of missing data information, which increases the difficulty of estimating the SOH of the battery. This requires that the selected features better reflect the battery aging process.

Incremental Capacity Analysis (ICA) is an important feature analysis method for battery SOH estimation [15], which is calculated by the following formula:

$$\frac{dQ}{dV} = \frac{I \times dt}{dV} = I \times \frac{dt}{dV} \quad (1)$$

where Q , I , V and t denote the capacity, current, voltage and time of battery charging, respectively.

When analyzing the charge/discharge voltage curves by traditional methods, it is difficult to accurately identify the starting and ending points of the voltage plateau due to the extremely small changes in the values, which makes it difficult to directly analyze the internal electrochemical reactions of the battery. In contrast, the IC curve constructed by

the ICA method is able to visualize the development of the voltage plateau and relate the external characteristics of the battery to the internal electrochemical performance, as shown in Figure 2a, where the peak position and height of the IC curve vary with the battery cycle number. Taking the highest peak of IC as an example, it represents the transition point where the phase transition occurs in the anode material of the battery, and the amount of lithium-ion material that can be embedded in the anode material within the unit voltage within this transition point is significantly elevated, so the IC curve shows a peak. As the battery ages, the highest peak appears to move the voltage to the higher voltage range and the peak value continues to decrease, indicating that the battery anode's ability to hold lithium-ions decreases. This characteristic is related to the growth of the solid electrolyte passivation film at the negative electrode of the battery and can be used to monitor the health of the battery and the aging process.

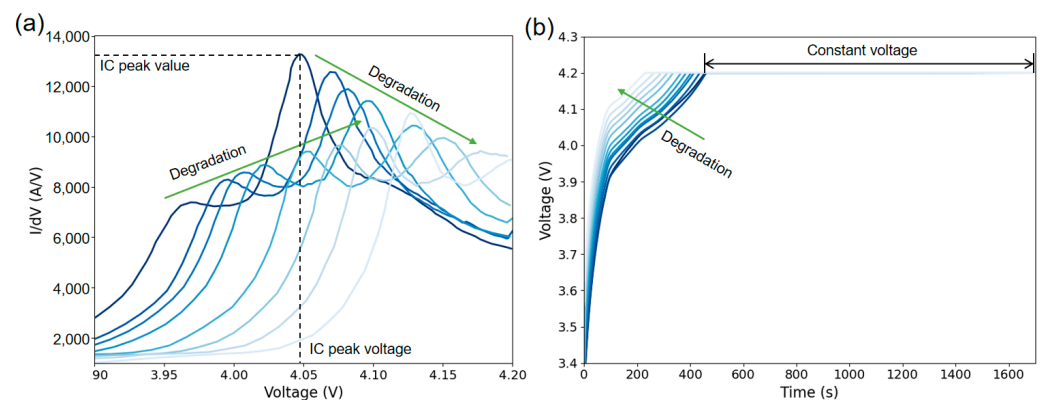


Figure 2. Feature analysis. (a) Evolution of IC curves. (b) Evolution of CVT curves.

When calculating the IC curves, fluctuations are introduced in the measured current and voltage due to sensor noise, which affects the feature extraction. To mitigate this effect, the Savitzky–Golay (SG) filtering method is used to smooth the IC curves. SG filtering is a smoothing filtering algorithm, which is based on the principle of smoothing the data by fitting a polynomial to the signal within a moving window while retaining the feature information (e.g., peak position). The core idea is to find the optimal polynomial coefficients within a sliding window of $2m + 1$ to minimize the error, which is calculated as follows:

$$y_i = \sum_{k=-m}^m c_k \cdot y_{i+k} \quad (2)$$

where y_i is the smoothed signal value. y_{i+k} is the point of the original signal in the window. c_k is the coefficient associated with the window weights. m is the half-width of the window. This series of weights c_k is obtained by fitting a polynomial within the sliding window using least squares.

Although ICA can effectively characterize battery aging, its computation involves differentiation and filtering processes, and the differentiation process tends to amplify the sensor noise, while the filtering may lead to the loss of key information, as well as a large computational cost. In addition, batteries exhibit complex performance characteristics under different operating conditions, which makes it difficult for a single feature to fully reflect their health status [32]. To address this limitation, we introduce different features to extract the internal information of the battery. This method improves the generalization ability of the model and enables it to better adapt to multiple usage scenarios.

To address this limitation, we propose an important feature: Constant Voltage Time (CVT). Due to the high dynamic uncertainty of the battery discharge condition, we extract features from the relatively stable CC-CV charging condition. For batteries in the switching

station, the SOC varies during incoming charging and maintenance, but the batteries in the switching station have sufficient time for recharge, usually by a complete constant voltage charging session. Figure 2b demonstrates the change of charging voltage curve during the aging of cell #1, which is charged with a 5C current in time, and its constant current link has not completely disappeared and has a complete constant voltage charging link. From the figure, we can also find that the constant voltage charging duration of the battery is increasing with the increase of the number of battery cycles, which indicates that it contains rich information about the aging of the battery. We extract the constant voltage charging time directly from the battery charging data without differentiation and filtering.

2.3. Deep Learning Approach

In this study we developed a deep learning framework for battery capacity estimation. As shown in Figure 3, the framework integrates a BiLSTM module with a Transformer module.

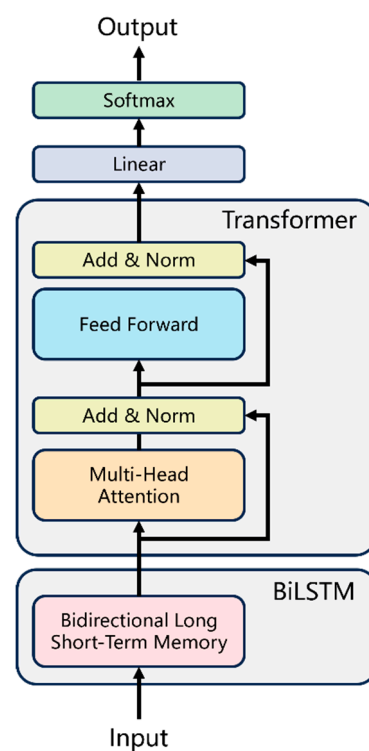


Figure 3. The flowchart of the deep learning method.

LSTM networks excel in processing time-series data, especially in the field of predicting the evolution of battery capacity over time. LSTM is able to capture long-term dependencies, which are critical for predicting battery SOH decay. Each LSTM cell consists of three gates (input, forgetting and output) and a cell state, which together regulate the information flow.

The role of the forgetting gate is to control what information is removed from the previous state. Its mathematical expression is

$$f_t = \sigma(W_{fx}x_t + W_{fH}h_{t-1} + b_f) \quad (3)$$

where x_t is the current input, h_{t-1} is the hidden state from the previous time step, W_{fx} and W_{fH} are the weight matrices of the forgetting gate, σ is the Sigmoid activation function, b_f is the bias term and f_t is the output of the forgetting gate.

The input gate controls the effect of the current input and the previous hidden state on the candidate cell state. It consists of two parts:

$$i_t = \sigma(W_{ix}x_t + W_{iH}h_{t-1} + b_i) \quad (4)$$

$$g_t = \tanh(W_{gx}x_t + W_{gH}h_{t-1} + b_g) \quad (5)$$

where W_{ix} , W_{iH} are the weight matrices of the input gates, W_{gx} , W_{gH} are the weight matrices of the candidate neuron states, and b_i and b_g are the bias terms of the input gates and candidate states.

The cell state is the core of the LSTM unit, which determines memory over long periods of time. The neuron state is updated by merging the outputs of the forgetting gate and the input gate:

$$c_t = c_{t-1}f_t + i_tg_t \quad (6)$$

where c_{t-1} is the cell state at the previous time step and c_t is the neuron state at the current time step.

The output gate determines the next hidden state and its mathematical expression is

$$o_t = \sigma(W_{ox}x_t + W_{oH}h_{t-1} + b_o) \quad (7)$$

$$h_t = o_t \tanh(c_t) \quad (8)$$

where W_{ox} and W_{oH} are the weight matrices of the output gates, b_o is the bias term, o_t is the output of the output gate and h_t is the output of the LSTM cell.

BiLSTM is a bi-directional architecture based on LSTM, where sequences are processed bi-directionally through two LSTM layers, forward and reverse, enabling the capture of richer contextual information. The prediction results of the forward and reverse LSTMs are merged and passed to the subsequent network layers. BiLSTM provides an improvement over traditional LSTM networks in capturing long-term dependencies with improved accuracy. For example, in the prediction of battery aging, the capacity decay process of the battery is not only related to the current state but also to multiple time steps in the past, and BiLSTM is able to consider these before and after dependencies simultaneously. In this study, we incorporate a layer of the BiLSTM network before the Transformer encoder to process the initial training features and generate more context-aware representations, which then provide a richer input to the subsequent Transformer module.

Transformer is a deep learning model based on an attention mechanism, originally used for natural language processing (NLP) tasks (e.g., machine translation), whose core feature is that it does not rely on recurrent networks (e.g., RNNs or LSTMs) to process sequential data, but instead uses self-attention and parallelized encoding–decoding architectures to achieve efficient modeling.

The architecture of Transformer consists of two main parts: the encoder and the decoder, which are composed of multiple stacked layers, respectively. Each layer includes the following main components: self-attention mechanism, feed-forward neural network (FFN), residual connection and layer normalization.

The self-attention mechanism allows the model to capture global dependencies by focusing on words at other positions in the sequence while encoding a word. The input sequence $\{x_1, x_2, x_3, \dots, x_n\}$ is mapped to an embedding vector with the addition of positional encoding to form a matrix $X \in R^{n \times d}$, where n is the length of the sequence and d is the embedding dimension. The Attention mechanism maps the input to query, key and value through three matrices:

$$Q = XW_Q, K = XW_K, V = XW_V \quad (9)$$

where W_Q, W_K, W_V are learnable weights.

To allow the model to capture different attention patterns, Transformer introduces the Multi-Head Attention mechanism:

$$\text{MultiHead}(Q, K, V) = \text{Concat}(\text{head}_1, \dots, \text{head}_h)W_O \quad (10)$$

$$\text{head}_i = \text{Attention}\left(QW_Q^i, KW_K^i, VW_V^i\right) \quad (11)$$

$$\text{Attention}(Q, K, V) = \text{softmax}\left(\frac{QK^T}{\sqrt{d_k}}\right)V \quad (12)$$

where h is the number of attention heads, W_O is the output transformation matrix, QK^T is the similarity matrix, $\sqrt{d_k}$ is a scaling factor that prevents the gradient from being too large and softmax is used to normalize the similarity values to probabilities.

After each attention mechanism, Transformer applies a position-independent feedforward neural network with two fully connected layers:

$$\text{FFN}(X) = \text{ReLU}(XW_1 + b_1)W_2 + b_2 \quad (13)$$

where W_1, W_2 are weights.

Each sub-layer (self-attention mechanism or FFN) is followed by residual connectivity and layer normalization, where residual connectivity helps gradient flow to avoid gradient vanishing, and layer normalization accelerates training and improves stability with the following expression:

$$\text{Output} = \text{LayerNorm}(X + \text{SubLayer}(X)) \quad (14)$$

The Transformer encoder consists of N layers of stacked submodules. The encoder output is a context-dependent representation of the sequence. The Transformer decoder is similar to the encoder, but its multi-head attention is hidden to prevent the decoder from viewing information about future locations. The decoder takes information from the output of the encoder. The Transformer total output formula can be expressed as follows: the encoder generates a contextual representation of the sequence H_{encoder} and the decoder generates the prediction Y_{output} based on the target input Y, H_{encoder} .

$$Y_{\text{output}} = \text{Decoder}(Y, H_{\text{encoder}}) \quad (15)$$

The specific steps of Transformer can be simplified as follows: compute the self-attention of the battery aging feature information transmitted from BiLSTM, weight the encoder outputs with attention and apply the feed-forward neural network to generate the final battery SOH estimation results. The hyperparameters of the model in this study are shown in Table 4.

Table 4. Configurations of the hyper-parameters range.

Hyper-Parameters	Value
look_back	100
output_sequence_length	1
epochs	100
num_features	3
embed_dim	4
dense_dim	8
num_heads	1
num_blocks	1

Table 4. Cont.

Hyper-Parameters	Value
dropout_rate	0.5
learn_rate	0.0002
batch_size	64
lstm_hidden_dim	4

3. Results and Discussions

3.1. Results of Feature Analysis

Considering the complexity of battery capacity degradation under different operating conditions, we first analyzed the correlation between three selected features and battery capacity. In this study, we used the Pearson correlation coefficient to quantify the previous correlation between the features and battery capacity. The Pearson correlation coefficient is a widely used measure of linear relationship, which defines the correlation coefficient between two variables X and Y as

$$\rho_{xy} = \frac{\sum_{i=1}^n (x_i - \bar{x})(y_i - \bar{y})}{\sqrt{\sum_{i=1}^n (x_i - \bar{x})^2} \sqrt{\sum_{i=1}^n (y_i - \bar{y})^2}} \quad (16)$$

where \bar{x} and \bar{y} denote the mean of the eigenvalues and battery capacity values, respectively, and n denotes the sample size. The correlation coefficient ρ_{xy} ranges from -1 to 1 , where values close to 1 or -1 indicate a strong relationship and values close to 0 indicate a weak relationship.

Figure 4 shows the correlation coefficients between the features extracted using the two methods and the battery capacity. The IC Peak Voltage as well as the CVT features extracted from the IC Analysis and CVT methods show high correlation coefficients, indicating that they are effective in capturing battery aging features, while the IC Peak Value correlation is somewhat lower. In this study, we select the above three features as input features for predicting battery capacity.

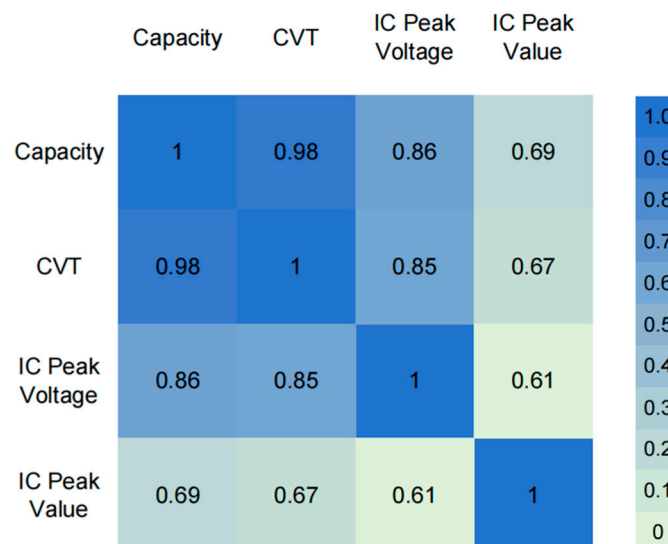


Figure 4. Correlation analysis results of multi-feature analysis.

3.2. Model Performance

In this study, we use the charging process data from the first 40% of the battery life cycle as a training set for model training, and 20% of the data as a validation set to reduce the risk of training overfitting. The capacity curve is estimated for the second 40% of the

battery lifecycle. The proposed model in this study estimates the capacity decay curves of 12 experimental sample batteries and characterizes the model performance by the RMSE between the real and estimated values, and the results are shown in Figure 5.

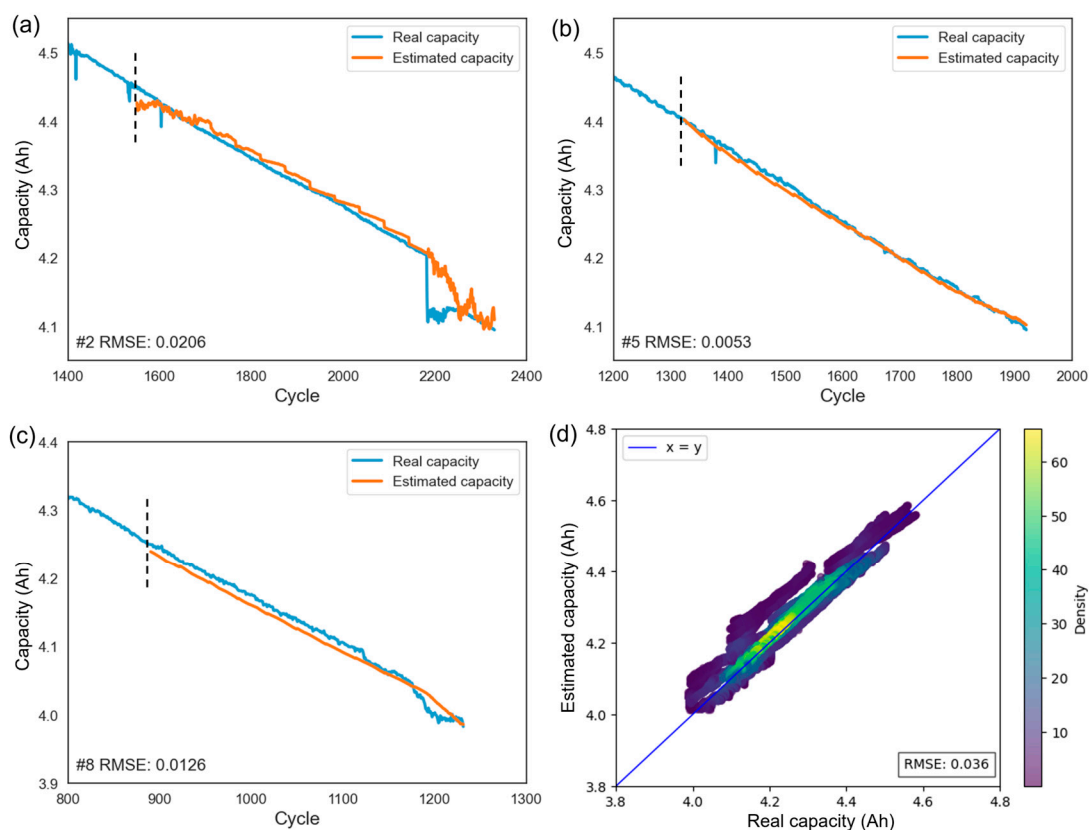


Figure 5. Battery capacity estimation results. (a–c) are the battery capacity decay curves. (d) Performance of the model on battery samples.

The proposed framework performs well in battery capacity estimation, with an RMSE below 0.04 Ah in most conditions, with the best case #5 achieving an estimation result of $\text{RMSE} = 0.0053$ Ah (normalized RMSE 0.11%) and the worst case #3 estimation $\text{RMSE} = 0.078$ Ah (normalized RMSE 1.6%). This result validates the effectiveness of the selected aging features and the robustness of the model training process.

Figure 5a,c shows the battery capacity decay curves, with the estimated values in orange and the real values in blue. For cell #5 with a high degree of linearity in the capacity curve, the model has a very high estimation accuracy, as shown in Figure 5b. Even if accelerated aging occurs at the EoL, as shown in Figure 5c, the model can accurately identify the accelerated decay of cell #8 under 0°C . In addition, if the battery shows capacity diving, as shown in Figure 5a, the model also captures the capacity diving behavior.

We estimate the capacity curve for each battery sample four times and plot the results in Figure 5d. The horizontal coordinate represents the real values and the vertical coordinate represents the estimated values, with colors closer to yellow representing denser data points and colors closer to purple representing sparser data points. It is noteworthy that the model still maintains high accuracy on the battery samples aged under multiple conditions, demonstrating its generalization ability in complex scenarios. This validates the effectiveness of the proposed CVT features and BiLSTM-Transformer-based framework in battery capacity degradation estimation.

3.3. Model Comparison

In order to evaluate the performance of the proposed BiLSTM-Transformer framework more rigorously, we conducted comparative experiments and RMSE error analyses of different types of models, as shown in Table 5. Support Vector Regression (SVR), a machine learning algorithm commonly used for regression problems, was often applied to battery SOH prediction in the past, and we chose SVR as a comparative model for estimating the effect. In addition, we selected the LSTM network in the BiLSTM-Transformer fusion framework as well as the Transformer framework as the control group. We use the above four networks/frameworks to estimate the battery with a high degree of SOH linearity (#5) and the battery with a low degree of SOH linearity (#2), respectively. So, the experimental groups all use the same features and are trained with the first 40% capacity curve of the battery, the 20% capacity curve is used as a validation set and the remaining 40% capacity curve is estimated.

Table 5. RMSE results of different models.

Method	#2	#5
SVR	0.0691 Ah	0.0222 Ah
LSTM	0.0589 Ah	0.0588 Ah
Transformer	0.0438 Ah	0.0162 Ah
BiLSTM-Transformer	0.0206 Ah	0.0053 Ah

The SVR and LSTM models achieved different prediction results on the two batteries; SVR predicts better than LSTM for batteries with a higher degree of linearity, but is slightly inferior on batteries with capacity jumps, as shown in Figure 6. The core idea of SVR is to regress the prediction by mapping the input data to a high-dimensional feature space and finding an optimal hyperplane in the high-dimensional space. For small and medium-sized datasets, SVR performs stably and with high computational efficiency. However, for large datasets, the training process of SVR may become more time-consuming. Since SVR is less capable of handling time-series data, especially when it needs to capture long-term dependencies, the performance of SVR is not as good as that of LSTM, so the prediction error of SVR is significantly lower than that of the highly nonlinear capacity decay curve (#2) for the simpler capacity decay curve (#5).

By applying the memory cells, LSTM can effectively capture long-term dependencies in sequences and is suitable for modeling complex time-series data, such as battery capacity trends (#2). This is the reason why LSTM models are increasingly used in battery state estimation compared to SVR models. Even though the LSTM model is capable of capturing the capacity dips, however, it still shows a large error at the end of the battery life, as shown in Figure 6a. Because LSTM requires a large amount of training data and computational resources, the training process is more complicated. For the prediction target with better linearity (#5), its prediction effect may not be as good as SVR.

The wide applicability and robustness demonstrated by Transformer and its derived models provide new ideas for battery capacity estimation. The results show that the best battery capacity estimation is obtained using the BiLSTM-Transformer framework, and the Transformer framework results are close to it, but the estimation error is slightly higher than the former. This indicates that the network fusion approach improves the framework performance, and the estimation accuracy is high regardless of the degree of linearity of battery capacity decay. The fusion method effectively combines the advantages of different features and reflects the aging characteristics of batteries more comprehensively.

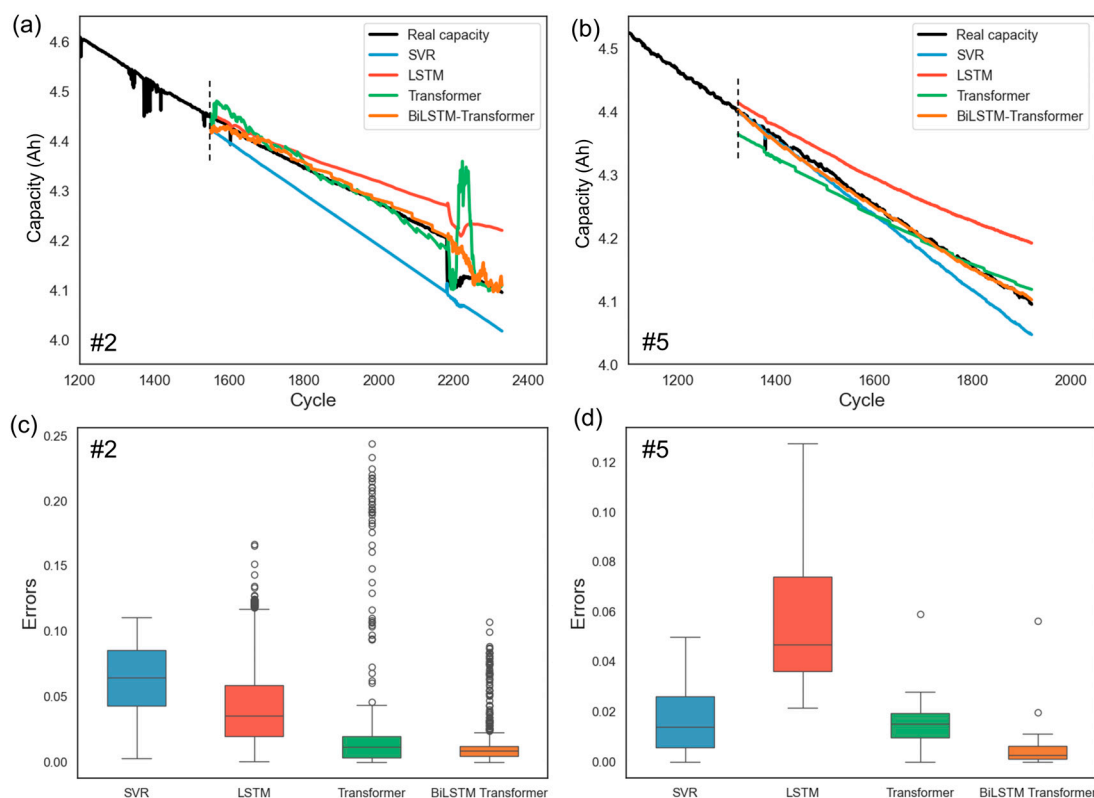


Figure 6. Comparative results for multiple types of models. (a) Cell #2 capacity estimation results. (b) Cell #5 capacity estimation results. (c) Cell #2 capacity estimation RMSE. (d) Cell #5 capacity estimation RMSE.

4. Conclusions and Outlook

4.1. Research Conclusions

This study presents a BiLSTM-Transformer framework for accurately estimating the capacity trajectory of LIBs under different operating conditions. The model adds a layer of BiLSTM network before the Transformer, which functions like an encoder, and utilizes the excellent ability of BiLSTM network to process time-series data to obtain the battery aging evolution characteristics over time and improve the framework estimation accuracy. Meanwhile, the Transformer, which combines the multi-attention mechanism, can learn the potential mapping relationship between the input data well to capture the key aging features from the voltage and current data. Meanwhile, in order to cope with the problem of missing battery discharge data for the swapping station, this study is based entirely on battery charging data. Capacity estimation operated under multi-temperature conditions is performed by extracting CVT features in combination with IC features traditionally used for battery capacity estimation.

Through correlation analysis, the CVT feature has a high correlation between capacity degradation and outperforms the classical IC feature. By combining the CVT features with the IC features, this study estimates the capacity of LIBs under 0 °C and 25 °C operating environments, both of which achieve good results. The BiLSTM-Transformer framework was used to estimate the capacity of the latter 40% of the battery under the condition of using 40% of the data as the training set and 20% of the data as the validation set. Most of the samples resulted in RMSE values below 0.04 Ah (normalized RMSE = 0.8%), and the worst estimate resulted in RMSE = 0.078 Ah (normalized RMSE = 1.6%). The estimation accuracy of the BiLSTM-Transformer framework is significantly higher than the LSTM model, as well as the Transformer. These results highlight the high accuracy, strong generalization

ability and adaptability of the framework proposed in this study. It provides a reliable and promising method for battery life estimation in power battery swapping stations to improve the operational efficiency and guarantee the safety and reliability of LIBs.

4.2. Future and Outlook

The proposed BiLSTM-Transformer framework marks a further development in the field of battery capacity estimation, especially under multiple battery operating conditions. However, further exploration is still needed in the following areas to enhance its robustness, generalization capability and practical applications.

During the peak battery swapping period, the short battery maintenance step at the swapping station may not allow full charging. It is difficult to obtain the CVT characteristics of the battery in the above cases. In the future, we can try to use the duration of the current change within the CV as a feature, such as the time when the current decreases from 0.5C to 0.1C, in order to cope with these kinds of small probability events, and to enhance the practicality of the framework.

The Transformer framework itself has a high complexity and powerful learning capability, but it is prone to overfitting and the robustness of the model is lacking in the case of a small training data size. Future research can use a multi-feature approach to increase its training data size, and further improve the model generalization ability by incorporating physical information features containing electrochemical principles, while reducing the risk of model training overfitting.

In addition, the adaptability to dynamic, real-time operating environments deserves further investigation. A lightweight model architecture is essential for integration into an embedded battery management system (BMS). The generalization of the model to solid-state batteries also warrants further investigation.

Author Contributions: Conceptualization, Y.S. and S.C.; methodology, H.X.; software, H.X. and X.L.; validation, X.W., H.X. and X.X.; formal analysis, S.C. and H.X.; investigation, Y.S. and X.X.; resources, Y.S. and X.W.; data curation, D.W.; writing—original draft preparation, Y.S. and H.X.; writing—review and editing, Y.S. and H.X.; visualization, X.W.; supervision, S.C. and J.W.; project administration, S.C.; funding acquisition, Y.S., X.W. and X.L.; All authors have read and agreed to the published version of the manuscript.

Funding: This research is funded by the special cost project of State Grid Jilin Electric Power Company Limited, “research on the state of health estimation of power batteries based on refined battery management” (SGJLJY00LNJS2400065).

Data Availability Statement: The original contributions presented in the study are included in the article, further inquiries can be directed to the corresponding author.

Conflicts of Interest: The authors declare that this study received funding from State Grid Jilin Electric Power Company Limited. The funder was not involved in the study design, collection, analysis, interpretation of data, the writing of this article or the decision to submit it for publication.

References

1. Lempert, J.; Kollmeyer, P.J.; He, M.; Haußmann, M.; Cotton, J.S.; Emadi, A. Cell selection and thermal management system design for a 5C-rate ultrafast charging battery module. *J. Power Sources* **2022**, *550*, 232121. [[CrossRef](#)]
2. Gao, Z.H.; Xie, H.C.; Yang, X.B.; Niu, W.F.; Li, S.; Chen, S.Y. The Dilemma of C-Rate and Cycle Life for Lithium-Ion Batteries under Low Temperature Fast Charging. *Batteries* **2022**, *8*, 234. [[CrossRef](#)]
3. Liu, J.; Chu, Z.; Li, H.; Ren, D.; Zheng, Y.; Lu, L.; Han, X.; Ouyang, M. Lithium-plating-free fast charging of large-format lithium-ion batteries with reference electrodes. *Int. J. Energy Res.* **2021**, *45*, 7918–7932. [[CrossRef](#)]
4. Huang, R.; Wang, X.; Jiang, B.; Chen, S.; Zhang, G.; Zhu, J.; Wei, X.; Dai, H. Revealing the electrochemical impedance characteristics of lithium-ion battery (nickel-cobalt-aluminum vs. graphite) under various alternating current amplitudes. *J. Power Sources* **2023**, *566*, 232929. [[CrossRef](#)]

5. Li, Z.; Fang, R.; Ge, H.; Liu, Z.; Spingler, F.B.; Jossen, A.; Zhang, J.; Liaw, B. Multiphysics Footprint of Li Plating for Li-Ion Battery and Challenges for High-Accuracy Detection. *J. Electrochem. Soc.* **2022**, *169*, 080530. [[CrossRef](#)]
6. Liang, Y.; Cai, H.; Zou, G. Configuration and system operation for battery swapping stations in Beijing. *Energy* **2021**, *214*, 118883. [[CrossRef](#)]
7. Adu-Gyamfi, G.; Song, H.; Obuobi, B.; Nketiah, E.; Wang, H.; Cudjoe, D. Who will adopt? Investigating the adoption intention for battery swap technology for electric vehicles. *Renew. Sustain. Energy Rev.* **2022**, *156*, 111979. [[CrossRef](#)]
8. Lei, Z.; Zhang, Y.; Lei, X. Improving temperature uniformity of a lithium-ion battery by intermittent heating method in cold climate. *Int. J. Heat Mass Transfer.* **2018**, *121*, 275–281. [[CrossRef](#)]
9. Xing, Y.; Ma, E.W.M.; Tsui, K.-L.; Pecht, M. An ensemble model for predicting the remaining useful performance of lithium-ion batteries. *Microelectron. Reliab.* **2013**, *53*, 811–820. [[CrossRef](#)]
10. Gao, K.; Sun, J.; Huang, Z.; Liu, C. Capacity prediction of lithium-ion batteries based on ensemble empirical mode decomposition and hybrid machine learning. *Ionics* **2024**, *30*, 6915–6932. [[CrossRef](#)]
11. Qin, T.; Zeng, S.; Guo, J. Robust prognostics for state of health estimation of lithium-ion batteries based on an improved PSO–SVR model. *Microelectron. Reliab.* **2015**, *55*, 1280–1284. [[CrossRef](#)]
12. Chaoui, H.; Ibe-Ekeocha, C.C. State of Charge and State of Health Estimation for Lithium Batteries Using Recurrent Neural Networks. *IEEE Trans. Veh. Technol.* **2017**, *66*, 8773–8783. [[CrossRef](#)]
13. Zhang, Y.; Xiong, R.; He, H.; Pecht, M.G. Long Short-Term Memory Recurrent Neural Network for Remaining Useful Life Prediction of Lithium-Ion Batteries. *IEEE Trans. Veh. Technol.* **2018**, *67*, 5695–5705. [[CrossRef](#)]
14. Shen, S.; Sadoughi, M.; Li, M.; Wang, Z.; Hu, C. Deep convolutional neural networks with ensemble learning and transfer learning for capacity estimation of lithium-ion batteries. *Appl. Energy* **2020**, *260*, 114296. [[CrossRef](#)]
15. Gao, Z.; Xie, H.; Yang, X.; Wang, W.; Liu, Y.; Xu, Y.; Ma, B.; Liu, X.; Chen, S. SOH estimation method for lithium-ion batteries under low temperature conditions with nonlinear correction. *J. Energy Storage* **2024**, *75*, 109690. [[CrossRef](#)]
16. Xu, X.; Tang, S.; Han, X.; Lu, L.; Wu, Y.; Yu, C.; Sun, X.; Xie, J.; Feng, X.; Ouyang, M. Fast capacity prediction of lithium-ion batteries using aging mechanism-informed bidirectional long short-term memory network. *Reliab. Eng. Syst. Saf.* **2023**, *234*, 109185. [[CrossRef](#)]
17. Yang, K.; Tang, Y.; Zhang, S.; Zhang, Z. A deep learning approach to state of charge estimation of lithium-ion batteries based on dual-stage attention mechanism. *Energy* **2022**, *244*, 123233. [[CrossRef](#)]
18. Ma, Y.; Li, J.; Gao, J.; Chen, H. State of health prediction of lithium-ion batteries under early partial data based on IWOA-BiLSTM with single feature. *Energy* **2024**, *295*, 131085. [[CrossRef](#)]
19. Li, Z.; Zhang, X.; Gao, W. State of health estimation of lithium-ion battery during fast charging process based on BiLSTM-Transformer. *Energy* **2024**, *311*, 133418. [[CrossRef](#)]
20. Bai, T.; Wang, H. Convolutional Transformer-Based Multiview Information Perception Framework for Lithium-Ion Battery State-of-Health Estimation. *IEEE Trans. Instrum. Meas.* **2023**, *72*, 2523312. [[CrossRef](#)]
21. Liu, X.; Yang, C.; Meng, Y.; Zhu, J.; Duan, Y. Capacity estimation of Li-ion battery based on transformer-adversarial discriminative domain adaptation. *AIP Adv.* **2023**, *13*, 075113. [[CrossRef](#)]
22. Spitthoff, L.; Vie, P.J.S.; Wahl, M.S.; Wind, J.; Burheim, O.S. Incremental capacity analysis (dQ/dV) as a tool for analysing the effect of ambient temperature and mechanical clamping on degradation. *J. Electroanal. Chem.* **2023**, *944*, 117627. [[CrossRef](#)]
23. Jones, C.; Sudarshan, M.; Tomar, V. Predicting the discharge capacity of a lithium-ion battery after nail puncture using a Gaussian process regression with incremental capacity analysis. *Energy* **2023**, *285*, 129364. [[CrossRef](#)]
24. Shibagaki, T.; Merla, Y.; Offer, G.J. Tracking degradation in lithium iron phosphate batteries using differential thermal voltammetry—ScienceDirect. *J. Power Sources* **2018**, *374*, 188–195. [[CrossRef](#)]
25. Ren, L.; Dong, J.; Wang, X.; Meng, Z.; Zhao, L.; Deen, M. A Data-Driven Auto-CNN-LSTM Prediction Model for Lithium-Ion Battery Remaining Useful Life. *IEEE Trans. Ind. Inform.* **2021**, *17*, 3478–3487. [[CrossRef](#)]
26. Yang, P.; Yang, H.; Meng, X.; Song, C.; He, T.; Cai, J.; Xie, Y.; Xu, K. Joint evaluation and prediction of SOH and RUL for lithium batteries based on a GBLS booster multi-task model. *J. Energy Storage* **2024**, *75*, 109741. [[CrossRef](#)]
27. Waldmann, T.; Hogg, B.I.; Wohlfahrt-Mehrens, M. Li plating as unwanted side reaction in commercial Li-ion cells—A review. *J. Power Sources* **2018**, *384*, 107–124. [[CrossRef](#)]
28. Chu, Z.; Feng, X.; Ouyang, M.; Wang, Z.; Lu, L.; Li, J.; Han, X. Optimal charge current of lithium ion battery. *Energy Procedia* **2017**, *142*, 1867–1873. [[CrossRef](#)]
29. Ren, D.; Smith, K.; Guo, D.; Han, X.; Feng, X.; Lu, L.; Ouyang, M.; Li, J. Investigation of Lithium Plating-Stripping Process in Li-Ion Batteries at Low Temperature Using an Electrochemical Model. *J. Electrochem. Soc.* **2018**, *165*, A2167–A2178. [[CrossRef](#)]
30. Attia, P.M.; Bills, A.; Planella, F.B.; Dechent, P.; Dos Reis, G.; Dubarry, M.; Gasper, P.; Gilchrist, R.; Greenbank, S.; Howey, D.; et al. Review—“Knees” in Lithium-Ion Battery Aging Trajectories. *J. Electrochem. Soc.* **2022**, *169*, 060517. [[CrossRef](#)]

31. Zhang, C.; Wang, Y.; Gao, Y.; Wang, F.; Mu, B.; Zhang, W. Accelerated fading recognition for lithium-ion batteries with Nickel-Cobalt-Manganese cathode using quantile regression method. *Appl. Energy* **2019**, *256*, 113841. [[CrossRef](#)]
32. Yang, X.; Xie, H.; Zhang, L.; Yang, K.; Liu, Y.; Chen, G.; Ma, B.; Liu, X.; Chen, S. Early-stage degradation trajectory prediction for lithium-ion batteries: A generalized method across diverse operational conditions. *J. Power Sources* **2024**, *612*, 234808. [[CrossRef](#)]

Disclaimer/Publisher's Note: The statements, opinions and data contained in all publications are solely those of the individual author(s) and contributor(s) and not of MDPI and/or the editor(s). MDPI and/or the editor(s) disclaim responsibility for any injury to people or property resulting from any ideas, methods, instructions or products referred to in the content.